Molding reflection from metamaterials based on magnetic surface plasmons

Shiyang Liu,[1,2] Wanli Lu,[2] Zhifang Lin,[2,3] and S. T. Chui[4]

[1]*Institute of Information Optics, Zhejiang Normal University, Jinhua, Zhejiang 321004, China*

[2]*State Key Laboratory of Surface Physics and Department of Physics, Fudan University, Shanghai 200433, China*

[3]*Key Laboratory of Micro and Nano Photonic structures (Ministry of Education), Fudan University, Shanghai, China*

[4]*Bartol Research Institute, University of Delaware, Newark, Delaware 19716, USA*

(Received 7 June 2010; published 12 July 2011)

We demonstrate a dramatically molded reflection of an electromagnetic (EM) wave from the magnetic metamaterial (MM) surface occurring near the magnetic surface plasmon (MSP) resonance. It is found that on one side of the source the reflected field nearly cancels the incoming field, giving rise to a shadowy region near the MM surface, while on the other side the reflected field considerably enhances the incoming field, resulting in a brightened region. Our analysis indicates that this effect arises from the coupling of the EM wave to the MSP band states which exhibit giant circulations going only in one direction due to the broken time reversal symmetry in MMs. Possible applications based on this effect are manifested in designing a robust one-way EM waveguide (OEMW), a 90° beam bender, and a beam splitter, which are shown to work even in deep subwavelength lateral scale ($\sim\lambda/10$), with λ the wavelength of the propagating EM wave. Furthermore, the dependence of the OEMW on the channel width, the robustness of the OEMW against the defect and disorder, and the tunability of the working frequency by an external magnetic field are also studied.

DOI: 10.1103/PhysRevB.84.045425 PACS number(s): 42.25.Bs, 41.20.Jb, 42.70.Qs, 85.70.Sq

I. INTRODUCTION

Plasmonic materials[1–4] are capturing increasing interest due to their promising applications ranging from nanophotonics and nonlinear optics, to biosensing and even medical therapy. Most efforts hitherto have been devoted to investigate the electric surface plasmons (ESP) originating from the collective resonance of electronic density wave and hosted by metallic building blocks. The symmetry of Maxwell's equations with respect to the magnetic and electric degrees of freedom enables a symmetric type of phenomenon in magnetic systems, which is known as "magnetic surface plasmon" (MSP),[5,6] which corresponds to the Damon-Eshbach mode.[7] In comparison with the ESP in the metallic system, the effect of the MSP due to the coupling of the electromagnetic wave and spin fluctuations in the magnetic system, esspecially in magnetic metamaterials (MMs), has not yet been well appreciated physically.

Besides the MSP effect, the magnetic system can actually offer more. Of particular interest is the effect resulting from the broken time reversal symmetry (TRS) under an external magnetic field (EMF). Over the last several decades, there has been much research on the effect of external field on the transport of electrons. An example is the quantized Hall effect.[8] The analog between Maxwell's equations and quantum mechanics has stimulated much interest in the relationship between phenomena involving electrons and photons. While much attention has been devoted to photonic band gap (PBG) materials[9] as an analog of the semiconductor, there have recently appeared burgeoning activities in exploring if related phenomena resulting from the TRS breaking for electrons can occur with photons. Among others, a skew scattering effect involving electromagnetic (EM) waves was observed and investigated by Rikken and coworkers;[10] the EM one-way edge modes analogous to quantum Hall edge states were revealed theoretically[11,12] and implemented experimentally[13,14] by use of magnetic photonic crystal (MPC).

Our research is motivated by exploring the EM properties of an MSP resonance in a magnetic system with TRS breaking. In this work, we report our study on the reflection behavior of the EM wave from a two-dimensional magnetic metamaterial (MM) slab consisting of an array of ferrite rods. We found that when a line source is placed near the surface of an MM slab, the reflected EM wave can be drastically shaped, such that the field appears dramatically different on opposite sides of the source. In addition, we anticipate that there will be different applications based on this sharply asymmetric reflection (SAR) effect.

The paper is organized as follows. In Sec. II, we explain the SAR effect and its physical origin. The dependence of the effect on the frequency and the source-interface separation is examined as well. In Sec. III, we present a design of a one-way EM waveguide (OEMW) based on this effect. In Sec. IV, we further examine the robustness of our OEMW against defect, disorder, and inhomogeneity of the EMF. The difference between the OEMW designed based on the SAR effect and that using the EM edge states is illustrated, and the role of the MSP resonance is identified. After that, in Sec. V we exhibit the tunability of OEMW by an EMF, a desirable property for practical applications. In Sec. VI, also based on the SAR effect, we design a nearly 100% efficient sharp beam bender and a beam splitter. It is demonstrated that the designed EM devices can be operable even in the deep subwavelength scale. Our results are summarized in Sec. VII.

II. SAR FROM AN MM SLAB

As shown in Fig. 1, the MMs considered are made of yttrium-iron-garnet (YIG) rods arranged periodically in a square lattice in air with the axes of the rods along the z direction. Later on, we shall also explore the size and position fluctuation of these rods. The lattice constant is $a = 8$ mm and

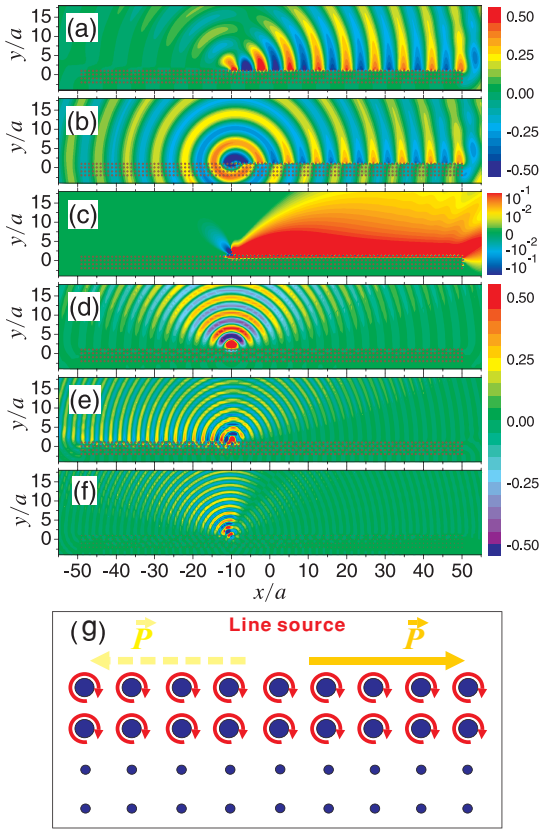

FIG. 1. (Color online) The profile of the total electric field (a), the scattered electric field (b), and the x component of the Poynting vector (c) when a line source with frequency $f = 5$ GHz close to the MSP resonance is placed near the surface of an MM slab. The lattice constant of the MM slab is $a = 8$ mm and the line source is located $1.0a$ away from the surface of the MM slab. The reflection behavior is also shown for the frequencies located at $f = 9.5$ GHz (d) and $f = 15.5$ GHz (e), corresponding to those in the lower and higher photonic band gaps, respectively, due to the Bragg scattering. For comparison, we simulate the reflection behavior (f) from an MPC slab with the same parameters in Ref. 12. We also present the simple physical picture (g) for the excitation of the one-way circulating MSP band states, which is responsible for the occurrence of the SAR in panels (a)–(c) and (e).

the radius of the YIG rod is $r = \frac{1}{4}a = 2$ mm. The magnetic permeability of the fully magnetized YIG rod is given by[15]

$$\hat{\mu} = \begin{bmatrix} \mu & -i\mu' & 0 \\ i\mu' & \mu & 0 \\ 0 & 0 & 1 \end{bmatrix}, \tag{1}$$

where the matrix elements μ and μ' are of resonance forms given, respectively, by

$$\mu = 1 + \frac{\omega_m(\omega_0 + i\alpha\omega)}{(\omega_0 + i\alpha\omega)^2 - \omega^2},$$

and

$$\mu' = \frac{\omega_m\omega}{(\omega_0 + i\alpha\omega)^2 - \omega^2},$$

with a spin wave resonance frequency $\omega_0 = 2\pi f_0 = 2\pi\gamma H_0$, determined by the sum of an EMF applied along the z direction and the anisotropy field; the gyromagnetic ratio $\gamma = 2.8$ MHz/Oe. $\omega_m = 2\pi f_m = 2\pi\gamma M_0$ measures the coupling strength of the magnetic material with the EM waves, with M_0 the saturation magnetization along the z direction. The damping is controlled by a coefficient α. For single crystal YIG, the saturation magnetization $M_0 = 1750$ Gauss, the damping coefficient $\alpha = 3 \times 10^{-4}$, and the permittivity $\varepsilon_s = 15 + 3 \times 10^{-3}\, i$.[16] We focus on the transverse magnetic (TM) wave with the electric field polarized along the rod axis.

For a ferrite rod with the permeability given by Eq. (1), the MSP resonance occurs at a frequency,

$$f_s = f_0 + \tfrac{1}{2} f_m, \tag{2}$$

corresponding to the case with $\mu + \mu' = -1$.[6] To explore the effects resulting from the combination of the MSP resonance and the TRS breaking, we have examined the reflection behavior of a TM wave excited by a line source oscillating at frequency near f_s and located near an MM slab composed of YIG rods. The simulation is performed using the rigorous multiple scattering method.[17–20] The incoming and the scattered fields are expanded in terms of basis states with different angular momenta.[21,22] Typical results are shown in Figs. 1(a)–1(c), where the line source oscillating at $f = 5$ GHz is located a distance a away from a four-layer MM slab. The applied EMF field is such that $H_0 = 900$ Oe, yielding $f_s = 4.97$ GHz. The total electric field, the scattered electric field, together with the x component of the Poynting vector are shown in panels (a)–(c), respectively. The SAR effect manifests itself in Fig. 1(a): On the left-hand side (LHS) of the line source, the scattered field substantially cancels the incoming field, resulting in a darkened region near the MM surface. On the right-hand side (RHS) of the line source, the scattered field significantly enhanced the EM field, giving rise to a brightened region near the MM surface. The SAR effect can be further understood with the help of the photonic band structure, as shown in Fig. 2. Around the MSP resonance, two

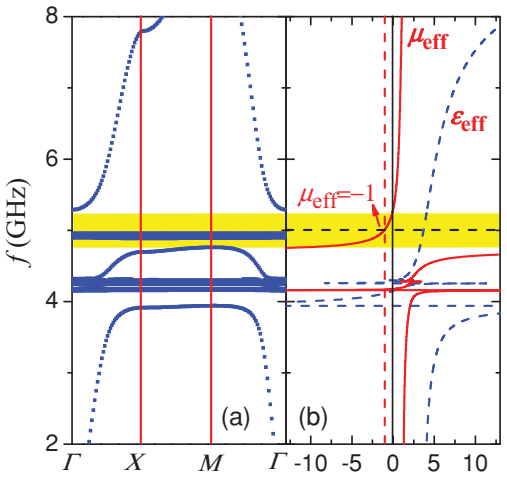

FIG. 2. (Color online) (a) The photonic band diagram of the MM with a square lattice configuration and under an EMF of $H_0 = 900$ Oe. (b) The effective constitutive parameters retrieved from the MM where the blue dashed line and red solid line correspond to the effective permittivity ε_{eff} and the effective magnetic permeability μ_{eff}, respectively.

PBGs come into existence, as denoted by the yellow stripes in Fig. 2(a). Accordingly, the EM wave cannot propagate inside the MM slab. The vanishment of the total field inside the MM slab implies that the incident and scattered fields inside the photonic crystal have a phase difference of π and cancel out each other. For the scattered wave, on the LHS of the line source, the bright fringes both inside and outside the photonic crystal shown in Fig. 1(b) remain at the same positions. This indicates that the scattered waves on the LHS are continuous in phase near the surface of MMs. As the scattered field cancels the incident field inside the MM slab, it therefore also attenuates the incident field outside the MM slab. The situation is quite different on the RHS of the line source. As can be seen from Fig. 1(b), the bright fringe outside the MPC slab is at the same place as the dark fringe inside the MPC slab along the interface. There appears a nearly half-wavelength mismatch for scattered waves inside and outside the MM slab. This suggests a phase change around π inside and outside the MM slab. As a result, while the scattered field cancels the incident field inside the slab due to the phase mismatch, it considerably enhances the EM field near the surface outside the slab owing to in-phase interference. This illustrates the SAR effect phenomenologically.

To understand the SAR effect further, we first examine the origination of the MSP resonance of the MMs. It depends on the resonance of each single ferrite rod occurring when $\mu + \mu' = -1$, which can be regarded as the effective permeability of a single ferrite rod. The coupling of the neighboring MSP resonant states of each single ferrite rod results in the resonance of the whole system. The resonance frequency was given in Eq. (2). At the working frequency $f = 5$ GHz (corresponding to the wavelength 60 mm) the wavelength is nearly 8 times the lattice constant a so that the MM can be considered as an effective medium. With the effective-medium theory developed in our previous work[23] we can retrieve the effective permeability tensor,

$$\mu_e = \begin{bmatrix} \mu_r & -i\mu_\kappa & 0 \\ i\mu_\kappa & \mu_r & 0 \\ 0 & 0 & 1 \end{bmatrix}, \tag{3}$$

whereas the effective permeability μ_{eff} for TM mode is given by $(\mu_r^2 - \mu_\kappa^2)/\mu_r$, which is shown in Fig. 2(b). We compare the photonic band diagram and the effective constitutive parameters. Double positive effective parameters correspond to the photonic bands, the single negative effective parameter corresponds to the photonic gap, while the resonances correspond to the flat bands where the physics is also affected by the off-diagonal element of the permeability tensor. Near the frequency corresponding to the flat bands in Fig. 2(b) (at the MSP resonance frequency $f_s = 4.97$ GHz) the effective magnetic permeability is nearly equal to -1 as is marked by the black dashed line, consistent with the analysis on the single ferrite rod. For this reason, the MSP resonance can be considered as the magnetic analog of the surface plasmon resonance inhabited in the metallic materials. In addition, the working frequency range (marked with the yellow stripe) lies in the frequency range where $\mu_{\text{eff}} < 0$, in the vicinity of the MSP resonance. The occurrence of the MSP resonance can lead to the excitation of the unidirectional circulation of the energy flow as schematically shown in Fig. 1(g). Accordingly, for a line source located near the surface of the MM slab, the leftward energy flow is inhibited while the rightward energy flow is supported and reinforced. For this reason, we can observe the SAR effect shown in Figs. 1(a) and 1(c). By reversing the orientation of the EMF the circulation of the energy flow can also be reversed so that the EM property of the SAR effect is magnetically tunable.

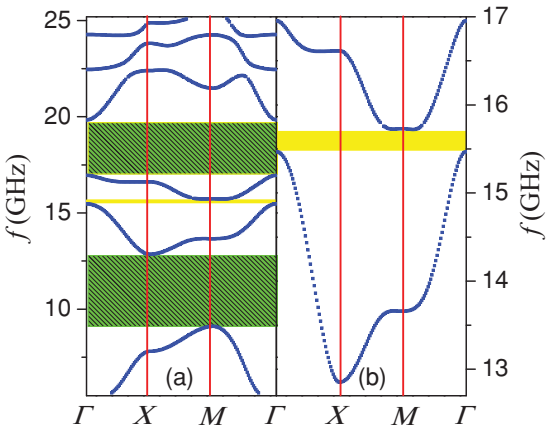

FIG. 3. (Color online) (a) The photonic band diagram at the higher frequency where three photonic band gaps can be found due to the bragg scattering. (b) The amplified view of the photonic band diagram around the second band gap. All the parameters involved are the same as those in Fig. 2.

Now we turn to explore the dependence of SAR effect on frequency. In Fig. 3(a), we present the photonic band diagram at higher frequencies, where three photonic band gaps are identified. We first examine the field pattern [Fig. 1(d)] at the frequency $f = 9.5$ GHz located at the bottom of the first PBG. This field pattern is almost symmetric; no SAR effect can be observed. Presumably, Chern numbers of the photonic bands nearby are zero, corresponding to a tiny circulation of the energy flow so that no significant asymmetry is observed. The result is consistent with that of Wang and coworkers' research where they present the Chern number corresponding to the photonic bands.[12] Similarly, for the topmost PBG ranging from 17 to 19.5 GHz, the SAR effect cannot be observed either for the same reason as the case shown in Fig. 1(d). Between these two PBGs, there exists another narrow PBG marked as a yellow stripe in Fig. 3(a). We select a frequency $f = 15.5$ Hz as the working frequency to examine the SAR effect. For convenience, we have given in Fig. 3(b) the amplified view of the photonic band diagram around the PBG. The electric field pattern for this case is shown in Fig. 1(e) where the electric field on the RHS is nearly vanished near the interface, while on the LHS the electric field can be supported so that the SAR effect comes into appearance.

For comparison, we have also simulated the reflection behavior of a line source from an MPC slab with the same parameters as in Wang and coworkers' research[12] (namely, with lattice constant $a = 38.7$ mm, radius of the ferrite rod $r = 0.11a = 4.3$ mm, the corresponding matrix elements of the magnetic permeability $\mu = 14$ and $\mu' = -12.4$, the working frequency $f = 4.28$ GHz, and the line source located $0.25a$ away from the interface). It can be observed from

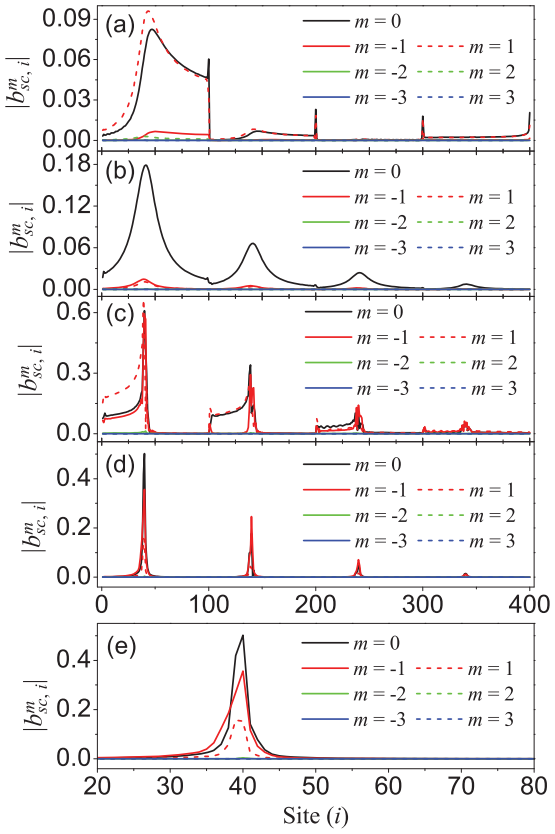

FIG. 4. (Color online) The scattering amplitude $|b^m_{sc,i}|$ of different angular momenta components at different positions for the line source located near MM slab. The panels (a)–(c) correspond to the cases in Fig. 1(a)–1(c), 1(d), and 1(e), respectively. The rod indices $i = 1 - 100$ correspond to the first layer, $i = 101 - 200$ the second layer, $i = 201 - 300$ the third layer, and $i = 301 - 400$ the fourth layer. (d) The scattering amplitude corresponding to the case in Fig. 1(f). (e) The amplified view of panel (d).

Fig. 1(f) that the EM wave is reflected somewhat leftward. In this case, the Chern numbers of the photonic bands around the PBG are not zero as shown by Wang and coworkers.[12] However, different from panels (a) and (e), there appears no enhancement of theEM field near the interface, which will be explained later.

To gain a deeper understanding of the SAR effect, we now examine the scattering amplitude $|b^m_{sc,i}|$ of the expansion partial waves corresponding to different angular momenta m at different positions i.[21,22] The results for the cases in Figs. 1(a)–1(c), 1(d), and 1(e) are presented in Figs. 4(a)–4(c), respectively. In panel (b), the scattering amplitude corresponding to the lowest order $m = 0$ is the largest; in addition, the amplitudes for the positive and the negative angular momenta are nearly equal, similar to the case for the EM wave scattered from a dielectric object. With the change of the rod indices i the scattering amplitude exhibits a nearly symmetric distribution. For this case, no SAR effect is observed as shown in Fig. 1(d). Differently, in panel (a) the largest scattering amplitude is that for the angular momentum $m = 1$, while the scattering amplitude for the angular momentum $m = -1$ nearly vanished. With the change of the rod index i, an apparently asymmetric distribution of $|b^m_{sc,i}|$ is manifested, which explains the SAR effect shown in Fig. 1(a). For the results shown in panel (c), the largest scattering amplitude is still that for $m = 1$. However, it can be seen that although the scattering amplitude for $m = -1$ is smaller, it is still comparable to that for $m = 1$. It is not suppressed as the case in Fig. 4(a). The reason lies in that at this frequency the MSP resonance cannot be excited. Consequently, although the SAR effect is demonstrated in Fig. 1(e), the electric field near the surface is much weaker. For comparison, we also calculate the scattering amplitude for a line source reflected from an MPC slab with the same parameters in Wang and coworkers' research.[12] The results are displayed in Fig. 4(d), corresponding to the field pattern shown in Fig. 1(f). To examine Fig. 4(d) clearly, we have shown in Fig. 4(e) its amplified view. It can be observed that the scattering amplitude for $m = 0$ is the largest, that for $m = -1$ it is a little smaller, while larger than that for $m = 1$. All the other terms are nearly zero. Due to the difference of the scattering amplitude for $m = -1$ and $m = 1$, a finite circulation of energy flow can be induced, leading to the asymmetric reflection shown in Fig. 1(f). The above analysis indicates that the SAR effect originates from the combined action of the TRS breaking of the MM system and the excitation of the MSP resonance. Due to the broken TRS, the scattered field consists of an unequal amount of states with opposite angular momenta m and $-m$. This inequality is greatly reinforced near the MSP resonance so that the angular momenta content are dominated by one sign, with the other sign almost suppressed. A giant circulation of energy flow therefore develops,[24] such that only energy flow in one direction is supported, while in the other (opposite) direction it is severely inhibited near the MM surface, as is manifested in Fig. 1(c). As a consequence, one side of the line source near the MM surface is brightened and the other side of the region is darkened.

It is interesting to note that the direction of EM energy circulation does not depend exclusively on the direction of magnetization, as can be seen by a comparison between Figs. 1(a) and 1(e). To determine the direction of the circulation (clockwise or anticlockwise) we need to calculate the circulation of the energy flow around the ferrite rods. For a single rod, it can be evaluated according to

$$\oint \boldsymbol{P} \cdot d\boldsymbol{l} = A(\omega) \sum_m m \left| \frac{b_m}{q_m} \frac{H_m^{(1)}(x)}{J_m(x)} - 1 \right|^2 |q_m J_m(x)|^2 , \quad (4)$$

where $A(\omega) = \frac{\pi |E_0|^2}{\mu_b \omega}$ is the prefactor with E_0 the amplitude of the incident wave and μ_b the magnetic permeability of the background medium, $x = k_b r$ is the size parameter, b_m and q_m are, respectively, the expansion coefficients of the scattered and incident wave corresponding to the angular momentum m, $J_m(x)$ is the Bessel function, and $H_m^{(1)}(x)$ is the Hankel function of the first kind. From Eq. (4), it can be found that the circulation of energy flow depends on the difference of the scattering amplitude for the $|m|$ and the $-|m|$ terms, while the scattering amplitude corresponding to $m = 0$ is not involved. We have calculated the circulation of energy flow around a typical ferrite rod in the first layer of the MM slab. The results show that the circulation is about $-10^{-2} A(\omega)$ for Fig. 4(a), suggesting a clockwise energy flow, thus explaining the rightward reflection in Fig. 1(a). For

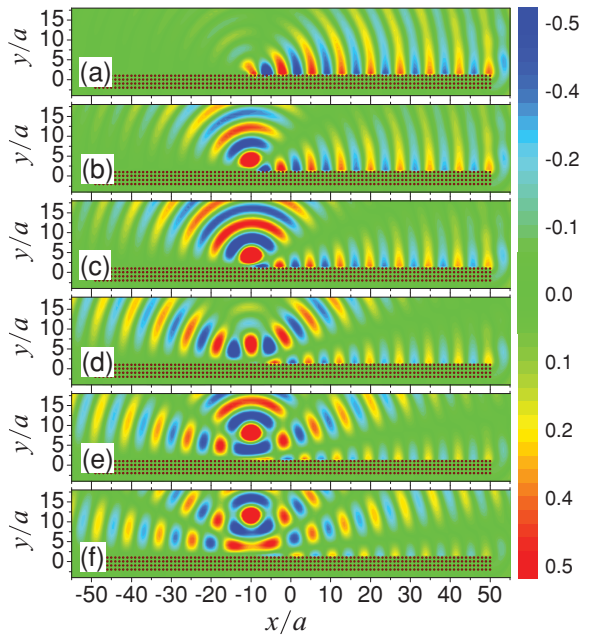

FIG. 5. (Color online) The electric field patterns of a line source radiating EM wave at the working frequency $f = 5$ GHz scattered from an MM slab for different source-interface separations d. Panels (a)–(f) correspond to the cases when $d = 1a, 2a, 3a, 5a, 7a$, and $10a$, respectively. All the other parameters are the same as those in Fig. 1.

Fig. 4(b), the circulation is nearly zero, corresponding to the nearly symmetric reflection in Fig. 1(d). For Fig. 4(c), the circulation is about $10^{-2}A(\omega)$, indicating that an anticlockwise energy flow is thus formed, explaining the leftward reflection in Fig. 1(e), while for the case in Fig. 4(d), the circulation is about $10^{-4}A(\omega)$, much weaker than Fig. 4(c). Accordingly, although the leftward reflection occurs, along the interface nearly no EM mode is supported. This explains the result shown in Fig. 1(f).

To examine the dependence of the SAR effect on the source-interface separation d, we have shown in Fig. 5 the electric field patterns for different d. Panels (a)–(f) correspond to the cases when $d = 1a, 2a, 3a, 5a, 7a$, and $10a$, respectively. The operating frequency is $f = 5$ GHz; all the other parameters of the MM slab are the same as those in Fig. 1. When the line source is close to the interface of the MM slab a dramatic SAR effect can be observed so that most electric field is scattered rightward. With the increase of the separation d, the SAR effect becomes weaker and weaker, namely, more and more electric field is scattered outside. When the line source is far enough from the interface ($d \approx \lambda$), the electric field near the interface becomes very weak so that most electric field is scattered outside and the electric field pattern is nearly symmetric as shown in Figs. 5(e) and 5(f). This result can be understood from the following approximate physical picture. The incoming electric field at a position $\boldsymbol{r}$ is given by $E_i(\boldsymbol{r}) = \exp[i\boldsymbol{k}\cdot(\boldsymbol{r} - \boldsymbol{e}_y d)]/|\boldsymbol{r} - \boldsymbol{e}_y d|$. The scattered wave is approximately of the spatial dependence of that from an image term $E_s(\boldsymbol{r}) = \mathrm{s}\exp[i\boldsymbol{k}\cdot(\boldsymbol{r} + \boldsymbol{e}_y d)]/|\boldsymbol{r} + \boldsymbol{e}_y d|$ where $\mathrm{s} = \pm 1$, depending on whether one is on the left or right of the source. For small d, there is a big cancellation between these two terms. As d is increased, this cancellation always remains at $y = 0$. But for other values of y, this cancellation becomes less obvious.

III. DESIGN OF A ONE-WAY EM WAVEGUIDE

Now we turn to explore possible applications of the SAR effect. The first example is based on the remarkable asymmetry of the Poynting vector as shown in Fig. 1(c). Because there exist PBGs around the MSP resonance,[6] corresponding to the negative effective permeability as shown in Fig. 2(b), the EM wave can be confined between two MM slabs, similar to the conventional photonic crystal waveguide.[25] If the magnetization of two MM slabs are in opposite directions, then the EM wave reflected forward from one MM slab will also be reflected forward from the other, leading to the design of a one-way EM waveguide (OEMW) different from those proposed recently.[11–14,26,27] This is illustrated in Fig. 6(a) where a line source is placed at $(-5.5a, 0)$, between two MM slabs $2a$ apart. The parameters for the MM slabs and the operating frequency of the line source are the same as in Figs. 1(a)–1(c). It can be seen that the wave propagates rightward from the x component P_x of the Poynting vector $\boldsymbol{P}$ as shown in Fig. 6(b). To further demonstrate the one-way characteristic, we display in Fig. 6(c) the electric field along $y = 0$ and the rightward transmitted power, $T_x = \int_{-3a}^{3a} P_x dy$, as a function of x. It can be seen that the EM energy transfers rightward, with $T_x > 0$, even on the LHS of the line source.[28] In addition, the EM energy exhibits an extremely low decay rate that is less than 0.1 dB/λ as it moves rightward when taking into account the realistic material absorption for single crystal YIG ferrite commercially available.[16] To illustrate basically the physical effect, in the following, we will neglect the damping for simplicity as in Ref. 12.

As shown in Fig. 5, the SAR effect is dependent on the separation of the line source to the interface. This suggests that the OEMW designed based on this effect also depends on the channel width. Physically, as the channel width becomes larger than a wavelength, some of the EM wave will just go parallel to the channel without going through a reflection and the unidirectional propagation characteristic as shown

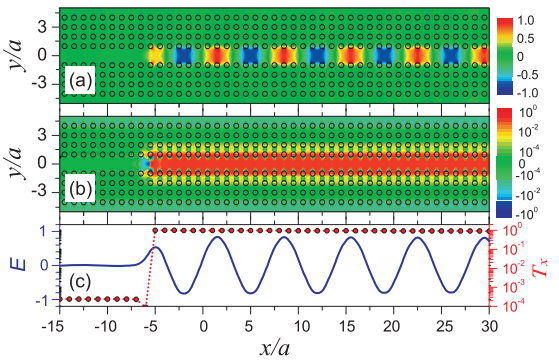

FIG. 6. (Color online) The electric field (a) and the x component of the Poynting vector (b) due to a line source of $f = 5$ GHz located at $(-5.5a, 0)$, between two MM slabs with opposite magnetization and $2a$ apart. Here $a = 8$ mm is the lattice constant of a square lattice of MMs. (c) Displays the electric field E (blue solid line) at $y = 0$ and rightward transmitted power T_x (red dotted line) versus x.

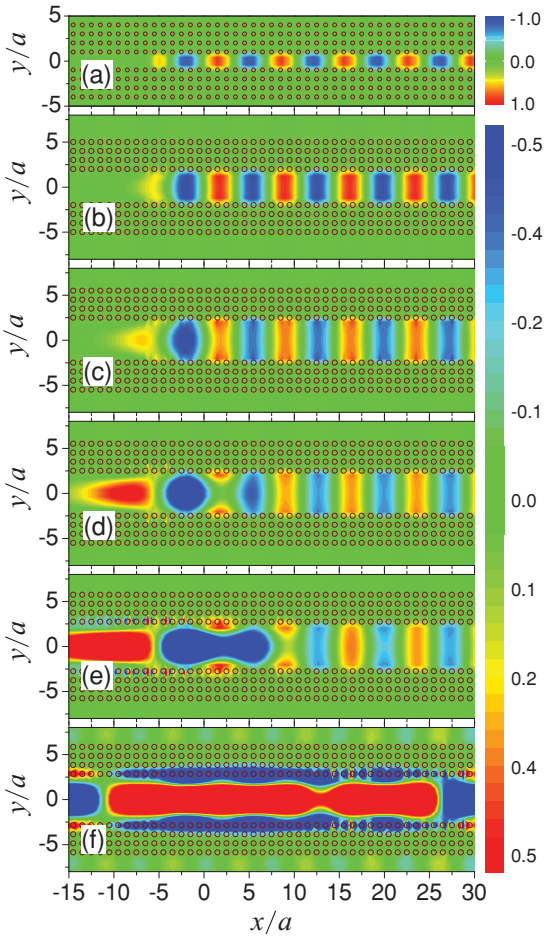

FIG. 7. (Color online) The electric field patterns of the OEMW with different channel widths. Panels (a)–(f) correspond to the cases for the channel widths $D = 2.0a$, $D = 4.0a$, $D = 5.5a$, $D = 5.6a$, $D = 5.7a$, and $D = 6.0a$, respectively.

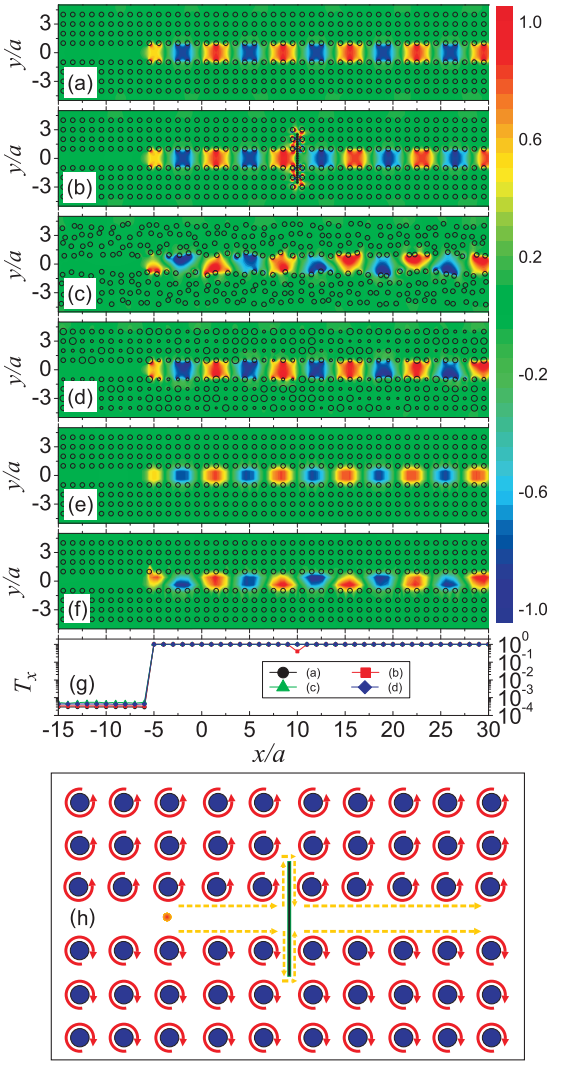

FIG. 8. (Color online) The electric field patterns for the OEMW under the conditions (a) the same as Fig. 6(a), given here for comparison, (b) with the introduction of a drastic PEC defect, (c) with position disorder, or (d) with size disorder. The inhomogeneity of the EMF is considered as well for the cases of (e) inhomogeneous and symmetric EMF, and (f) inhomogeneous and asymmetric EMF. It can be seen that in all circumstances the one-way propagating of the EM wave is kept. In addition, we have shown the normalized transmitted power versus x for (a)–(d) in panel (g). The physical picture for (b) is schematically shown in (h).

in Fig. 6 will be diminished. In Fig. 7, we have presented the electric field patterns for the OEMW with different channel widths. Panels 7(a)–7(f) correspond to channel widths $D = 2.0a$, $D = 4.0a$, $D = 5.5a$, $D = 5.6a$, $D = 5.7a$, and $D = 6.0a$, respectively. For channel width $D < 5.5a$ the OEMW works well; the leftward propagating EM wave is suppressed completely. However, with the increase of the channel width more and more EM field leaks leftward as shown in Figs. 7(d)–7(f). This is consistent with the result shown in Fig. 5 in that the SAR effect becomes weaker and weaker with the increase of source-interface separation. When the separation $D = 6.0a$, with our finite length sample, no obvious difference can be observed for the leftward and rightward propagating EM waves as can be seen from Fig. 7(f).

IV. ROBUSTNESS OF OEMW AGAINST DEFECT, DISORDER, AND INHOMOGENEITY

Another important issue of current interest is the robustness of a design against defect and disorder. Our numerical simulations indicate that the one-way propagation based on the SAR effect appears immune to defect and disorders, as is illustrated typically in Figs. 8(b)–8(d). Figure 8(b) gives the electric field pattern when a finite linear array of close-packed perfect electrical conductor (PEC) rods is inserted into the channel. The radius of the PEC rod is $r_p = \frac{1}{8}a$. The linear array ranges from $y = -2.5a$ to $y = 2.5a$, implying a drastic defect extending over $\frac{2}{3}\lambda$ in size. The wave is seen to circumvent the PEC defect, maintaining complete power transmission with T_x staying basically unchanged along the channel, as shown in Fig. 8(g). The schematic diagram shown in Fig. 8(h) could be helpful for the understanding of the mechanism dominating the behavior. Due to the MSP resonance near the working frequency, a strong circulation of the energy flow around each single rod can be excited. Accordingly, the channel can only support the energy flow in one direction, while in

the opposite direction it is completely suppressed. When a PEC defect is inserted into the channel, an equivalent channel can be created between the defect and the MMs as shown by the dashed vertical arrows. Accordingly, the energy flow can still get around the PEC defect by propagating along this equivalent channel, resulting in the nearly complete energy transmission. By comparing with the defect-free waveguide shown in Fig. 8(a), it can be seen that the defect changes only the phase of the rightward propagating wave, as a result of the delay due to the defect.

Our OEMW is also robust against the fluctuation of the rod size and the rod position. In Figs. 8(c) and 8(d), we present, respectively, the corresponding electric field patterns for these two types of disorder. Position disorder is introduced by allowing the coordinates of each rod to vary by a maximum amount equal to $\frac{1}{4}a$. The fluctuation in radius is uniform up to 50% of the unperturbed radius. The disorder only alters the wave patterns, but not the power transmission through the channel [see Fig. 8(g)]. Actually, for an even stronger position or size fluctuation the OEMW still works well provided that the channel is not destroyed. For the edge state waveguide,[12] the working frequency lies in the Bragg type of band gap; it suffers from the disorder of the building blocks in the MPCs. This demonstrates the difference in physics between metamaterials and MPCs.

In a realistic situation, the EMF cannot be homogeneous. For this reason, we also present the electric field patterns for the OEMW under an inhomogeneous EMF. Figure 8(e) corresponds to the case when a symmetric EMF is exerted. The EMFs at the different layers from inside to outside are, respectively, 890 Oe, 910 Oe, 930 Oe, and 950 Oe, symmetrically for the upper and lower slabs. The situation corresponding to the asymmetric inhomogeneous EMF is also considered as shown in Fig. 8(f) where the EMFs at different layers (from inside to outside) are 870 Oe, 900 Oe, 910 Oe, 950 Oe for the upper slab and 920 Oe, 930 Oe, 940 Oe, 970 Oe for the lower slab. It can be seen that the symmetric distribution of the EMF leads to a symmetric electric field pattern and the asymmetric EMF shaped the electric field pattern into the asymmetric one. However, a good performance can still be maintained. This is also a favorable aspect for the practical applications of the EM devices.

For comparison, we demonstrate in Fig. 9 the vulnerability for the OEMW designed with operating frequency deviating away from the MSP resonance. The MPC slab that supports unidirectional wave propagation has the same parameters as the case shown in Fig. 1(f). We present simulation results for two different configurations of OEMW. The first one was that suggested by Wang and coworkers, namely, with an introduction of cladding layer made of photonic band gap material to confine the EM wave to the MPC edge, as shown in Fig. 9(a), where the auxiliary cladding layer is made up of nearly touching PEC rods. The second configuration is the case considered in the present work, based on two MPC slabs with opposite directions of magnetization and $1.5a$ apart, as shown in Fig. 9(b). It can be seen from Figs. 9(a) and 9(b) that for perfect MPC, the EM wave propagates leftward, both exhibiting excellent unidirectionality. However, both configurations of OEMW suffer from position disorder and the size fluctuation of ferrite rods. This is shown in Figs. 9(c)–9(f).

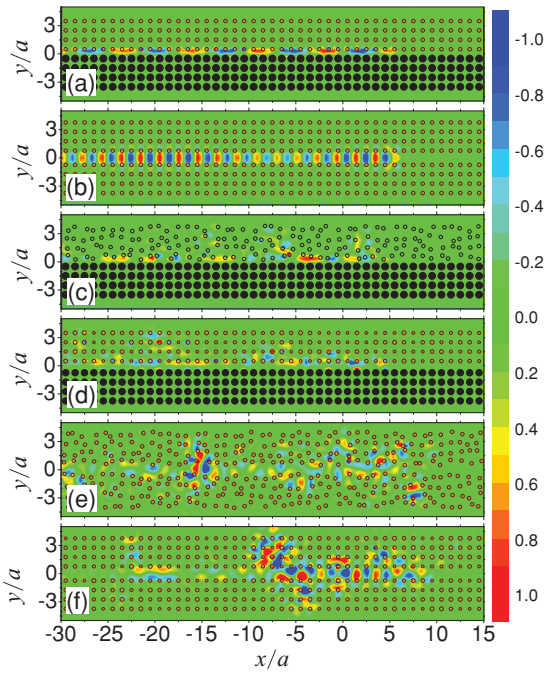

FIG. 9. (Color online) (a) The electric field patterns for the OEMW with the configuration as in Wang and coworkers' research (Ref. 12). The ferrite rods are marked by the hollow circles and the solid circles denote the PEC rods. Panels (c) and (d) demonstrate, respectively, the results with the introduction of position and size disorder in the MPC slab. The parameters of the MPC are the same as those in Fig. 1(f). For comparison, the OEMW constructed in our configuration with the channel width $D = 1.5a$ is shown in (b) for the case without disorder, and the cases with the introduction of position disorder (e) and the size disorder (f).

Figure 9(c) displays that when a moderate position disorder is introduced, much EM energy leaks outside the channel from the MPC slab, ruining the OEMW based on Wang's configuration. For the size fluctuation, even if it is very weak, the EM wave can still leak outside, resulting in the destruction of the OEMW as shown in Fig. 9(d). For the OEMW with the configuration considered in our work, the situation is similar for the working frequency (4.28 GHz) deviating away from the MSP resonance. The results are shown in Figs. 9(e) and 9(f), corresponding to the introduction of position disorder and size fluctuation of the ferrite rods, respectively. Compared with the OEMW designed based on the MSP resonance (see Fig. 8), it is obvious that the MSP resonance plays a very important role in developing the immunity of the system from defect and disorder. The reason lies in that the MSP resonance induced PBGs do not depend strongly on the periodicity. In addition, the MSP resonance frequency is determined by the magnetic permeability of the ferrite rod, independent of its size. Based on the effect shown in Fig. 1(e), we can also design an OEMW. However, the one-way propagating property is also vulnerable to position and size disorder due to the absence of the MSP resonance, similar to that given in Fig. 9.

V. TUNABILITY OF THE OEMW BY AN EMF

A special property of the OEMW based on the MSP resonance is the tunability of the working frequency by an

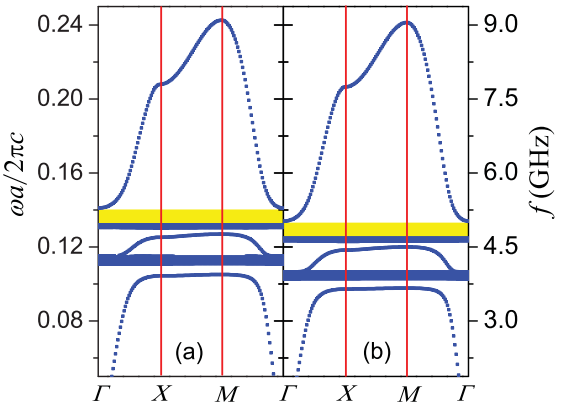

FIG. 10. (Color online) The photonic band diagrams of the MMs with a square lattice configuration and under EMFs of (a) $H_0 = 900$ Oe and (b) $H_0 = 800$ Oe, respectively. The parameters of the MMs are the same as those used in Fig. 6. The working frequency ranges for the OEMW under different EMS are denoted with the yellow stripes.

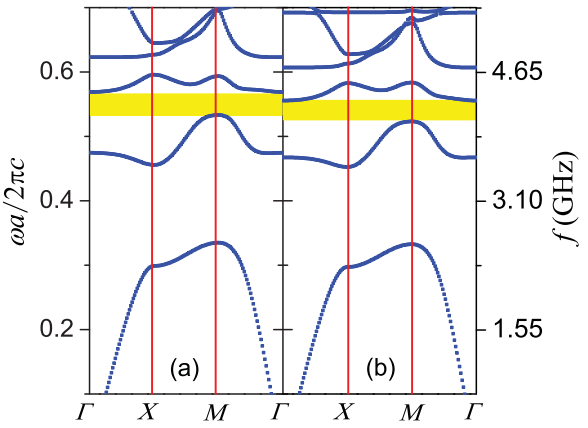

FIG. 12. (Color online) The photonic band diagrams of an MPC under $H_0 = 1600$ Oe (a) and $H_0 = 1500$ Oe (b), respectively. The MPC has the parameters that are the same as those in Wang and coworkers' research. Differently, in our case the dispersion of the ferrite rod is considered.

EMF. This tunability of the MSP resonance can be seen from the photonic band diagrams of the MMs under different EMFs $H_0 = 900$ Oe and $H_0 = 800$ Oe in Figs. 10(a) and 10(b). The yellow stripes mark the working frequency range of the OEMW; the flat bands there correspond to the MSP resonance. When the EMF decreases from $H_0 = 900$ Oe to $H_0 = 800$ Oe, the flat bands move downward; so does the working frequency. In this manner, we can manipulate the working frequency with an EMF. In Fig. 11, we present the electric field patterns of the OEMW under $H_0 = 900$ Oe [(a) and (b)] and $H_0 = 800$ Oe [(c) and (d)], respectively. In panel (a), the frequency is $f = 5.2$ GHz, lying in the working frequency range, and the other parameters of the OEMW are the same as those in Fig. 6. The EM field is confined in the channel and a good one-way propagating behavior is manifested. When the frequency is changed to $f = 4.7$ GHz, lying outside the working frequency range, the EM field leaks outside the channel as shown in Fig. 11(b). The EM field becomes weaker and weaker as it propagates along the channel so that at this frequency it cannot be used as an OEMW. Nonetheless, by tuning the EMF to $H_0 = 800$ Oe, $f = 4.7$ GHz is located in the new working frequency range as can be seen from Fig. 10(b). It can be seen that the OEMW still works well as shown in Fig. 11(c). Similar to the result shown in Fig. 11(b), if the frequency is tuned to $f = 5.2$ GHz most of the EM field leaks outside the channel for $H_0 = 800$ Oe as shown in Fig. 11(d). The above results suggest that by tuning the EMF from $H_0 = 900$ Oe to $H_0 = 800$ Oe, the working frequency can be adjusted from 5.2 GHz to 4.7 GHz. Accordingly, by tuning the EMF we can manipulate the working frequency of the OEMW.

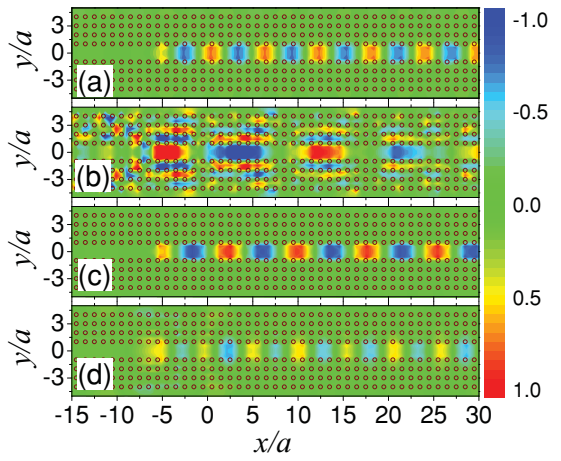

FIG. 11. (Color online) The electric field patterns for the OEMW working at frequency $f = 5.2$ GHz (a), (d) and $f = 4.7$ GHz (b), (c). The exerted EMFs are $H_0 = 900$ Oe and $H_0 = 800$ Oe for (a) and (b) and (c) and (d), respectively. All the other parameters are the same as those in Fig. 6.

For comparison, we have also considered the tunability of the OEMW designed in Wang and coworkers' research based on the edge state at the PC-MPC interface. The corresponding photonic band diagrams under $H_0 = 1600$ Oe and $H_0 = 1500$ Oe are presented, respectively, in Figs. 12(a) and 12(b). Different from the results shown in Fig. 10, only a tiny shift of the working frequency is demonstrated by comparing the positions of the yellow stripes in Figs. 12(a) and 12(b). The working frequency is not easily tuned by an EMF. The results suggest once again that the MSP resonance plays an important role in designing the OEMW. The manipulability of the EMF on the OEMW can also be manifested by changing the propagating direction through reversing the orientation of the magnetization.

VI. DESIGN OF A BEAM BENDER AND SPLITTER

Based upon the SAR effect, we can also find other applications such as the EM waveguiding in the presence of a sharp bend. A typical example of such applications is illustrated in Fig. 13 where the configuration of the system is similar to that of the OEMW except that a cladding slab is added on top of the system. For a line source located at $(0, -15a)$, the EM wave is seen to propagate upward, while the downward propagating EM modes are completely

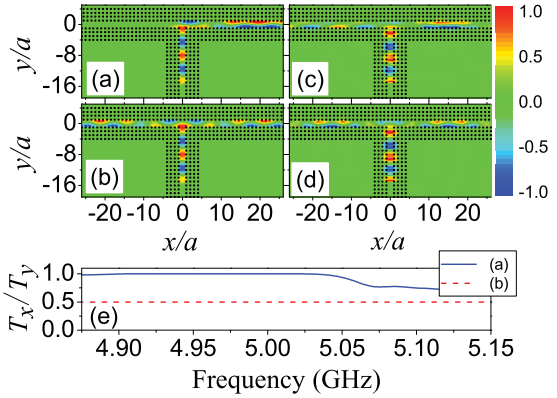

FIG. 13. (Color online) The electric field patterns showing a 90° beam bender (a) and a beam splitter (b) working at $f = 5$ GHz under the EMF $H_0 = 900$ Oe. The lattice constant is $a = 8$ mm, kept unchanged and the line source is located at $(0, -15a)$; (c) and (d) correspond to the electric field patterns at the frequency $f = 5.1$ GHz. The curves in (e) give the transmissivity T_x/T_y as the functions of frequency with T_x and T_y denoting the rightward and upward transmitted power in the right channel and the vertical channel, respectively.

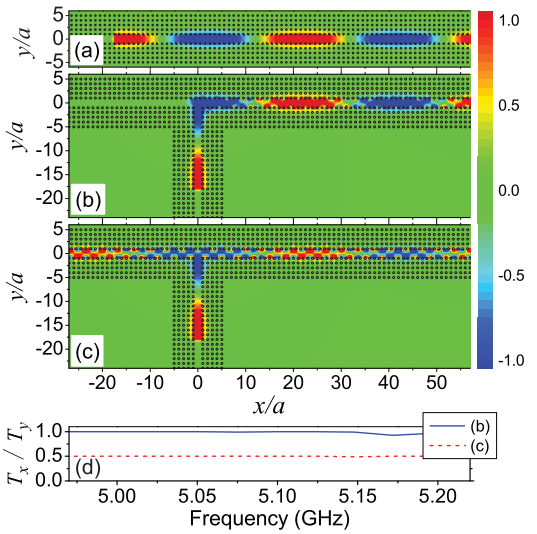

FIG. 14. (Color online) (a)–(c) The same as Figs. 6(a), 13(a), and 13(b), respectively, except that the lattice constant of the MMs is $a = 2$ mm and rod radius $r = \frac{1}{4}a$. The curves in (d) correspond to the rightward transmissivity defined in the same manner as that in Fig. 13(e).

suppressed. After that, the EM waves make a 90° turn at the corner with nearly 100% power transmission, as shown in Fig. 13(e) in more quantitative detail. We defined power transmission rates as T_x/T_y with T_x and T_y the EM energy transferred along the two different parts of the channel in the x (rightward) and the y (upward) directions. They are calculated numerically according to $T_x = \int_{-3a}^{3a} P_x dy$ and $T_y = \int_{-3a}^{3a} P_y dx$. By reversing the magnetization of the rods with coordinates $x < 0$ in the upper cladding slab, the EM wave can be divided equally into two branches at the bifurcation point $x = 0$ as shown in Fig. 13(b). In each wing the EM wave propagates with 50% power transmission in some frequency range, as is shown in Fig. 13(e) by the red dashed line. The EM wave experiences an extremely low reflection at the corner of the bend and the splitter, as can be seen from the field pattern in the vertical channel before bending and splitting and from Fig. 13(e). In the frequency range $f > 5.04$ GHz the power transmission rate for the beam bender decreases obviously as is shown in Fig. 13(e). To explain this, we have presented the electric field patterns for the beam bender and splitter at the frequency $f = 5.1$ GHz as shown in Figs. 13(c) and 13(d), respectively. For the beam bender, due to the difference of the light path at the upper and lower interfaces the wave front is severely distorted. The light path at the upper interface is longer than that at the lower interface. In addition, as the frequency deviates from that of the MSP resonance, the circulation of the energy flow becomes weaker. Therefore, some part of the EM wave leaks leftward as shown in Fig. 13(c), resulting in the drop of the transmission rate. Since the orientation of the magnetization can be controlled by an EMF, the function of the system can be switched between bender and splitter. This makes the device more flexible and favorable in practical applications.

Photonic circuits with no backscattering based on the SAR effect can be achieved even in deep subwavelength scale. Figure 14 shows such an example. The systems considered are the same as those in Figs. 6(a), 13(a), and 13(b), respectively, except that the MM is scaled down in size, with $a = 2$ mm and $r = \frac{1}{4}a$, while keeping the working frequency $f = 5$ GHz unchanged. In this case, the wavelength $\lambda = 60$ mm is nearly 30 times the lattice constant a. A superior subwavelength confining and steering is exhibited in a straight OEMW, a sharp beam bender, and a beam splitter. Our numerical simulations indicate that the full lateral width at half maximum field intensity $w_h < 0.1\lambda$. The transmissivity is presented in panel (d) for the beam bender and splitter as denoted by the red dashed line and the blue solid line, respectively. It can be seen that the EM devices exhibit a high transmission efficiency as well as a finite band width. Comparing Fig. 14(d) with Fig. 13(e), a shift of the working frequency is also demonstrated, which arises from the enhancement of the coupling strength due to the decrease of the separation between the ferrite rods. From Fig. 14(d), we find that the transmission efficiency for the beam bender is much improved since the decrease of the channel width will ease up the distortion of the field pattern as can be observed in Fig. 14(b). The leakage of the EM wave to the LHS of the horizonal channel decreases as well. Besides, just like the case shown in Fig. 13 the function of the system is still magnetically switchable between beam bender and splitter.

VII. CONCLUSION

In summary, based on the MSP resonance and the TRS breaking nature of MMs we have discovered an SAR effect near the interface of an MM slab. The phenomenon has been interpreted from the aspects of the photonic band diagrams and the scattering amplitude of the expansion partial waves. The dependence of the phenomenon on the frequency and the source-interface separation has also been examined. Possible applications are presented including a straight OEMW

immune to defect and disorder, a sharp beam bender, and a beam splitter, all with nearly complete power transmission. The dependence of the OEMW on the channel width has been examined as well. By comparing with the OEMW due solely to the TRS breaking, the role of MSP resonance has been established and the robustness and tunability of the OEMW based on the fusion of TRS breaking and MSP resonance have been demonstrated. In particular, it is shown that these applications can even be realizable in the deep subwavelength scale as well.

ACKNOWLEDGMENTS

This work is supported by the China 973 program (Grant No. 2011CB922004), National Natural Science Foundation of China (Grants No. 10774028 and No. 10904020), Ministry of Education of China (Grant No. B06011), State Science and Technology Commission (Grant No. 08dj1400302), China Postdoctoral Science Foundation (Grant No. 200902211), and Zhejing Normal University Initiative Foundation. S.T.C. is partly supported by the US Department of Energy.

[1] W. L. Barnes, A. Dereux, and T. W. Ebbesen, Nature (London) **424**, 824 (2003).
[2] A. V. Zayats, I. I. Smolyaninov, and A. A. Maradudin, Phys. Rep. **408**, 131 (2005).
[3] S. A. Maier, *Plasmonics: Fundamentals and Applications* (Springer, New York, 2007).
[4] F. J. G. de Abajo, Rev. Mod. Phys. **79**, 1267 (2007).
[5] J. N. Gollub, D. R. Smith, D. C. Vier, T. Perram, and J. J. Mock, Phys. Rev. B **71**, 195402 (2005).
[6] S. Y. Liu, J. J. Du, Z. F. Lin, R. X. Wu, and S. T. Chui, Phys. Rev. B **78**, 155101 (2008).
[7] R. W. Damon and J. R. Eshbach, J. Phys. Chem. Solids **19**, 308 (1961); A. Hartstein, E. Burstein, A. A. Maradudin, R. Brewer, and R. F. Wallis, J. Phys. C **6**, 1266 (1973).
[8] R. E. Prange and S. M. Girvin (editors) *The Quantum Hall Effect* (Springer-Verlag, Berlin, 1987).
[9] J. D. Joannopoulos, S. G. Johnson, R. D. Meade, and J. N. Winn, *Photonic Crystals: Molding the Flow of Light*, 2nd ed. (Princeton University Press, Princeton, 2008).
[10] G. L. J. A. Rikken and B. A. Van Tiggelen, Nature (London) **381**, 54 (1996).
[11] F. D. M. Haldane and S. Raghu, Phys. Rev. Lett. **100**, 013904 (2008).
[12] Z. Wang, Y. D. Chong, J. D. Joannopoulos, and M. Soljačić, Phys. Rev. Lett. **100**, 013905 (2008).
[13] Z. Wang, Y. D. Chong, J. D. Joannopoulos, and M. Soljačić, Nature (London) **461**, 772 (2009).
[14] Y. Poo, R. X. Wu, Z. F. Lin, Y. Yang, and C. T. Chan, Phys. Rev. Lett. **106**, 093903 (2011).
[15] D. M. Pozar, *Microwave Engineering*, 3rd ed. (Wiley, New York, 2005).
[16] E. P. Wohfarth, in *Ferromagnetic Materials* (North-Holland, Amsterdam, 1986).
[17] D. Felbacq, G. Tayeb, and D. Maystre, J. Opt. Soc. Am. A **11**, 2526 (1994).
[18] S. Y. Liu and Z. F. Lin, Phys. Rev. E **73**, 066609 (2006).
[19] S. Y. Liu, W. K. Chen, J. J. Du, Z. F. Lin, S. T. Chui, and C. T. Chan, Phys. Rev. Lett. **101**, 157407 (2008).
[20] S. Y. Liu, W. L. Lu, Z. F. Lin, and S. T. Chui, Appl. Phys. Lett. **97**, 201113 (2010).
[21] C. F. Bohren and D. R. Huffman, *Absorption and Scattering of Light by Small Particles* (Wiley, New York, 1983).
[22] H. C. van der Hulst, *Light Scattering by Small Particles* (Dover, New York, 1981).
[23] J. F. Jin, S. Y. Liu, Z. F. Lin, and S. T. Chui, Phys. Rev. B **80**, 115101 (2009).
[24] S. T. Chui and Z. F. Lin, J. Phys. Condens. Matter **19**, 406233 (2007).
[25] A. Mekis, J. C. Chen, I. Kurland, S. H. Fan, P. R. Villeneuve, and J. D. Joannopoulos, Phys. Rev. Lett. **77**, 3787 (1996).
[26] Z. Yu, G. Veronis, Z. Wang, and S. Fan, Phys. Rev. Lett. **100**, 023902 (2008).
[27] J. X. Fu, R. J. Liu, and Z. Y. Li, Appl. Phys. Lett. **97**, 041112 (2010).
[28] The EM energy on the LHS of the line source moves rightward because a small part of the EM wave circulates around the slab. As the sample size in the simulation increases, this tiny rightward energy flow decreases.